Heliyon 9 (2023) e13541

Contents lists available at ScienceDirect

Heliyon

journal homepage: www.cell.com/heliyon

Research article

Multi-objective optimization method for coil current waveform of transcranial magnetic stimulation

Ziqi Zhang [a], Chang Liu [c], Jihui Hu [b,*], Hongfa Ding [a], Zhou He [a], Yongxiu Song [a], Jiannan Shao [a], Dandi Zhang [a]

[a] Wuhan National High Magnetic Field Center, School of Electrical and Electronic Engineering, Huazhong University of Science and Technology, Wuhan, China
[b] School of Mathematics and Statistics, Huazhong University of Science and Technology, Wuhan, China
[c] Changjiang Institute of Survey, Planning, Design and Research, Wuhan, China

ARTICLE INFO

Keywords:
Transcranial magnetic stimulation
MOPSO
Joule heating
Vibration energy
Membrane potential
Intracranial induced electric field

ABSTRACT

Transcranial magnetic stimulation (TMS) has been proved to be effective in the treatment of many kinds of mental diseases. However, the clicking noise produced by the pulse current with large amplitude and short duration in the TMS coil may damage the hearing of patients. The heat produced by the high-frequency pulse current in the coil also reduces the efficiency of TMS equipment. A multi-objective waveform optimization method to improve heat and noise problems at the same time is presented. By analyzing the current waveforms of TMS, the relationship between the current and the vibration energy/Joule heating is established. Taking the Joule heating and the vibration energy as the optimization objectives, exceeding the same amount of neuronal membrane potential as the limiting condition, the Pareto fronts of different current models are obtained by applying the multi-objective particle swarm optimization algorithm (MOPSO). Therefore, the corresponding current waveforms are inversely deduced. A ringing suppression cTMS (RS-cTMS) proof-of-principle experimental platform is constructed. The feasibility of the proposed method is validated through experiments. The results show that the optimized current waveforms can greatly reduce the vibration and heating of the coil compared with the conventional full-sine, recified sine and half-sine waveforms, thus reducing the pulse noise and prolonging the using time of the equipment. The optimized diversified waveforms also provide a reference for the diversity of TMS.

1. Introduction

Transcranial magnetic stimulation (TMS) is a non-invasive, comparably safe neuro-modulation technique. By generating a time-varying magnetic field of the pulsed current in the coil, the intracranial induced electric field caused by the magnetic field is imposed on the external tissue of the brain structure. Currently, TMS is widely used in the clinical diagnosis and treatment of various neurological and mental diseases, as well as exploratory research in the field of brain science and cognitive science [1–6].

The application of TMS has a broad prospect, but there are still some problems that hinder the development of TMS. A large number of the existing research related to TMS concerns the design of the TMS coil structure or the pulse generator of TMS equipment, which

* Corresponding author.
E-mail address: hujihui@hust.edu.cn (J. Hu).

https://doi.org/10.1016/j.heliyon.2023.e13541
Received 14 July 2022; Received in revised form 27 January 2023; Accepted 1 February 2023
Available online 5 February 2023
2405-8440/© 2023 The Authors. Published by Elsevier Ltd. This is an open access article under the CC BY-NC-ND license (http://creativecommons.org/licenses/by-nc-nd/4.0/).

aims at improving the focality, stimulating depth, power supply efficiency and diversity of intracranial induced electric field [7–10]. While, this paper focuses on the problems of the coil heat and acoustic noise. The pulse current typically used to generate TMS can peak at several thousand amps, and this high current creates a non-negligible amount of heat on the coil due to the coil resistance. If the coil temperature rises too fast, it may damage the equipment and cause danger to patients and medical staff [11,12]. For the sake of safety, the pulses number of repetitive transcranial magnetic stimulation (rTMS) has to be limited. Along with the TMS pulse current, the coil will also make clicking sound due to the electromagnetic force, which may cause hearing damage [13–15]. At the same time, because of the nonlinearity and the large number of interactions in the brain, the click deteriorates the focus of the TMS [16,17]. The noise may also make the patient restless, upset and anxious, thus greatly affecting the treatment effect [18].

To deal with the problem of coil heat, some scholars have improved the efficiency of stimulation by changing the coil structure such as modifying the geometry [19] or adding iron-core to reduce the heat generation [20,21]. In addition, Ref. [22] uses an external heat sink to reduce heat accumulation on coils. Furthermore, the authors of Ref. [23] designed a hollow coil with circulation of deionized water to accelerate coil heat dissipation. Ref. [11] provides a current truncating circuit design used in some controllable pulse width TMS systems to reduce the coil heat.

On noise suppression, the current methods are mainly divided into two directions, waveform optimization and coil design [24]. There is also a part of research that uses active or passive methods to attenuate the noise heard by patients from the perspective of the sound receiver. Ref. [25] proposes a new double-containment coil with enhanced winding mounting to suppress the noise. Ref. [26] reduces the Lorentz self-force on the coil surface by a new coil optimization design to reduce the noise. Ref. [27] introduces a two-pronged solution by shortening the pulse width to make the dominant frequency components of the TMS noise above the human hearing and redesigning the coil. Ref. [28] proposes a method of using active noise control.

It can be seen that both the problems of coil heat and noise can be solved from the perspective of current waveform and coil structure. There are still fewer articles focusing on the former than on the latter. In this paper, we hope to improve the problems of coil heat and noise at the same time from the aspect of current waveform optimization, which has not been done to the author's knowledge. Ref. [29] optimizes the TMS current waveform with the single goal of reducing coil heat. The waveform parameterization is based on spline curves and Fourier series, whose degrees of freedom are handed over to hybrid global-local optimization algorithm. The optimization gives good results, but is very processor demanding and may be difficult to reproduce for a certain number of researchers. Besides, there are relatively few studies on TMS waveform optimization. We want to provide a more implementation-friendly multi-objective waveform optimization method to guide the TMS circuit construction, and the waveform parameterization is carried out with considerations more specific to TMS, which will be described in Section B of Chapter II. The multi-objective particle swarm optimization (MOPSO) algorithm, which is computationally more efficient among stochastic evolutionary algorithms with global search capability, is used [30–32].

Firstly, the mechanism of vibration noise and coil heat is described, the relationship between current, the vibration energy and Joule heating is obtained. Based on the characteristics of various TMS stimulation currents, the waveforms are modeled respectively. Then the neuronal membrane potential (MP) is used to judge the effectiveness of stimulation waveform. Subsequently, the Pareto fronts of waveforms are obtained by MOPSO algorithm, hence the optimized current waveforms are obtained. Finally, recommendations for circuit design are given based on the optimization results, and a proof-of-principle experimental platform was built to verify the realizability of the optimized waveform.

2. Method

2.1. Optimization objectives and constraints

It should be noted that since our focus is on the waveform, we first default the resistance in the circuit to be the same for all waveforms. In order to reduce the heat and vibration of the coil at the same time, two optimization objectives of current are defined.

2.1.1. Joule heating

The heat loss of the coil is mainly Joule heating. For coil current, the expression for Joule heating is expressed as [29]:

$$w_{heat} = \int RI^2 dt \propto \int I^2 dt \tag{1}$$

where the Joule heating w_{heat} is related to the coil resistance R and current I. The resistance is fixed in this paper thus the Joule heating in Eq. (1) is only related to the current.

2.1.2. Vibration energy

The fast-changing pulse current in the coil produces a large electromagnetic force. The force drives the coil to vibrate regularly and causes the clicking noise. Biot-Savart formula and Ampere force formula is expressed as:

$$dB = \frac{\mu_0}{4\pi} \cdot \frac{Idl \sin\theta}{r^2} \tag{2}$$

$$dF = Idl \times dB \tag{3}$$

where dB is the magnetic flux density, and Idl is the unit current, r is the distance from the measuring point of dB to the Idl, θ is the angle between the Idl and the unit vector of the Idl pointing to the location of dB, μ_0 is the magnetic conductivity. It can be deduced from Eqs. (2) and (3) that the instantaneous electromagnetic force dF of each turn is proportional to the square of the coil current I [28], and $F(t)$ represents the change of dF on the coil with time:

$$dF = F(t) \propto (Idl)^2 \tag{4}$$

The current in the TMS coil is discontinuous. In each pulse cycle, the duration of pulse lasts for hundreds of microseconds. Correspondingly, the duration of the electromagnetic force is the same as pulse, but the duration of noise is far longer than the pulse time. This is because the inevitable system damping exists in the actual vibration. When the electromagnetic impact force stops, the system vibrates freely according to the natural frequency. The vibration displacement response of the system at time t is obtained by performing Duhamel integral [33] on the electromagnetic force in Eq. (4):

$$x(t) = \frac{1}{\omega_d m} \int_0^t F(\tau) e^{-\frac{c}{2m}(t-\tau)} \sin \omega_d (t-\tau) d\tau \tag{5}$$

where c is the viscous damping coefficient, m is the mass of equivalent vibrator, $\omega_n = \sqrt{k/m}$ is the natural circle frequency of the system in undamped state, k is the stiffness, $\omega_d = \omega_n \sqrt{1-\sigma^2}$ is the actual vibration circle frequency of the system when the damping coefficient is c, and $\sigma = c/2\sqrt{km}$ is the damping ratio of the system. The expressions for the above parameters are the original defining equations in the field of vibration theory, and the parameters take different values for different coil structures, which can be extracted by simulation or measured experimentally. The parameters in this paper are extracted in COMSOL by performing the mechanical analysis and acoustic simulation of the coil and selecting the most representative finite element points as the equivalent point sources of noise. Further refinement of the study after determining the optimization results can be done directly using COMSOL and MATLAB for joint simulations, instead of using this simplified equivalence method.

Coil vibration drives other media to vibrate, thus converting kinetic energy into noise and sound energy. Therefore, the control of the coil vibration reduces the clicking noise at the roots. The Fourier integral transform of $x(t)$ in Eq. (5) is performed to find the frequency components of the vibration after decomposition into simple harmonic vibration, and the average energy flow density of each component is expressed as:

$$w^{--} = \frac{1}{2} \rho A^2 \omega^2 u \tag{6}$$

where ρ is the media density, A is the harmonic vibration amplitude, and ω is the angular frequency of the harmonic vibration, u is the length in the direction of the vibration wave velocity of the taken medium volume. Superimpose the average energy density of each frequency component in Eq. (6), to obtain the average energy density of the whole coil vibration, that is, the sound intensity, an acoustic indicator of vibration energy:

$$\overline{w}_{sum} = \sum_i \overline{w}(i) \tag{7}$$

where i is the order of Fourier series, $\overline{w}_{sum}$ in Eq. (7) is used to represent the vibration energy of TMS coil.

2.1.3. Voltage constraint

Larger di/dt will produce the greater induced electric field in the targeted stimulation site. But the coil voltage is also proportional to di/dt:

$$U_L = L \frac{di}{dt} \tag{8}$$

where L is the coil inductance, U_L in Eq. (8) is the coil voltage. For safety reasons, the coil voltage should not be too high, otherwise, the coil might get damaged. However, once the coil current changes, the coil voltage will shift. The problem of coil voltage rise is usually solved by adding Zylon fiber for better insulation. Consequently, a certain margin should be kept on the basis of the original coil voltage.

2.1.4. Action potential constraint

The action potential is the process of membrane potential change based on resting potential, when excitable cells are stimulated. The essence of TMS is to produce an action potential in targeted cells, so as to regulate cell excitability [34,35]. In this paper, the membrane potential (MP), assuming that the resting potential is 0, is used to represent the neurostimulation strength, and a larger MP magnitude signifies stronger neural stimulation [9]. Exceeding the set threshold of the MP, action potential generation, produced by the current is taken as another constraint.

In order to obtain the MP, the neuronal membrane is modeled as a leaky integrator (LI) to simulate the response to the sub-threshold stimulation, referring to Ref. [9,36–38]. The circuit model of the LI model can actually be considered as a first-order low-pass filter, and the induced electric field acting on the neuronal model is equivalent to passing the induced electric field through this first-order low-pass filter, which is implemented in MATALB using the *filter* function. The output of the *filter* is the

membrane potential [9,38]. The time constant τ_m of the filter depends on the biophysical characteristics of the stimulated neuronal membrane. It changes with age, gender, disease, drug effect, therapeutic effect and other factors of the patient [9]. It is set as 150 μs in this paper [37]. It should be noted that the MP obtained with this model may be slightly biased when measuring the stimulus intensity of different waveforms [38], and is therefore only a rough estimate of the stimulus intensity. This approximation is adopted to initially determine the waveform effectiveness within an acceptable error range to improve the efficiency of the study and to provide a basis for further studies on more detailed models to follow. The focus of this paper is on the proposed optimization ideas and methods, so a simpler neuronal model is used before specific optimization results are obtained. If the researchers have already specified the optimization direction when using the method proposed in this paper, they can simply replace the LI model with more detailed one as appropriate.

2.2. Current fitting model

The TMS coil current is usually half-sine, monophasic, biphasic or full-sine waveform. Relevant research shows that different current waveforms will cause different stimulation effects on the human body [39]. Therefore, it is necessary to model the TMS waveform first. Since most of the TMS waveforms of existing products are closer to trigonometric functions, we first use trigonometric functions as the basis functions for the waveform fitting. In this way, it is easier to summarize the optimization direction based on the differences between the obtained optimization results and the existing product waveforms, and the optimized waveform is also more achievable. Based on the second Stone-Weierstrass theorem, that is, the pulse waveform of TMS can be scaled to an odd function whose period is 2π, and the current waveform is fitted as:

$$f(x) = D + \sum_{n=1}^{\infty} A_n \sin(B_n x + C_n) \tag{9}$$

Further, the triangular fit optimization results give us an optimization orientation of shorter pulse widths, which, combined with some previous works on novel TMS for near-rectangular electric fields [9,29], leads us to wonder whether switching to a polynomial basis with a flatter derivative curve for waveform fitting would give us more optimization orientation, so we introduce the polynomial basis. As long as the polynomial order is high enough and the parameters are selected properly, the polynomial series of Eq. (10) is able to fit any current waveform. Based on the first Stone-Weierstrass theorem, continuous functions on closed intervals can be uniformly approximated by polynomial series, that is, any continuous function is fitted as:

$$f(x) = a_n x^n + a_{n-1} x^{n-1} + \cdots + a_1 x + a_0 \tag{10}$$

Consequently, several different approximation models are proposed in this paper as follows.

2.2.1. Piecewise polynomial series (Model.1a/1b1c)

According to the characteristics of TMS current waveform, the polynomial in Eq. (11) divides the TMS current waveform into three segments, in which $0 \sim e_1$ is the first segment, $e_1 \sim e_2$ is the second segment and $e_2 \sim t$ is the third segment. Each cubic polynomial is enough to fit one segment of the TMS waveform. Three different TMS current waveforms (i.e., biphasic double peak (BDP, Model.1a), monophasic double peak (MDP, Model.1 b), monophasic single peak (MSP, Model.1c) are obtained by controlling the zero-crossing points and trend of waveforms.

$$f_1(x) = \begin{cases} a_1x^3 + b_1x^2 + c_1x + d_1 & (0 \le x < e_1) \\ a_2x^3 + b_2x^2 + c_2x + d_2 & (e_1 \le x < e_2) \\ a_3x^3 + b_3x^2 + c_3x + d_3 & (e_2 \le x < t) \end{cases} \tag{11}$$

2.2.2. Trigonometric series (Model. 2a/2b/2c)

The full-sine current is the most commonly used waveform in TMS. The sinusoidal model as shown in Eq. (12) is considered to be connected by two different functions, similar to the form of Eq. (9), where e_1 and t are zero crossing points of the waveform. By controlling zero-crossing points and waveform trend, three trigonometric series models are established: biphasic sine (Model. 2a), rectified sine (Model. 2b), half-sine (Model. 2c).

$$f_2(x) = \begin{cases} D_1 + A_1 \sin(B_1x + C_1) & (0 \le x < e_1) \\ D_2 + A_2 \sin(B_2x + C_2) & (e_1 \le x < t) \end{cases} \tag{12}$$

2.3. Multi-objective particle swarm optimization

In some engineering problems, many objectives need to be optimized at the same time. Such objectives are mutually exclusive, that is, the increase of one objective results in the reduction of other objectives. In this paper, two objectives need to be optimized, i.e., Joule heating and vibration energy, which are not directly related. They may conflict with each other in the process of optimization. The mathematical model of multi-objective optimization problem is described as follows:

$$\begin{aligned} &Minimize \quad y = g(x) = (g_1(x), g_2(x), \ldots, g_m(x)) \\ &subject\ to \ \ h_i(x) \le 0, i = 1, \ldots I \\ &\quad k_j(x) \le 0, j = 1, \ldots J \\ &\quad x_m^{(L)} \le x_m \le x_m^{(U)} \end{aligned} \tag{13}$$

where x is the decision vector and y is the goal vector. $h_i(x)$ and $k_j(x)$ are inequality and equality constraints respectively. $x_m^{(L)}$ and $x_m^{(U)}$ represent the lower and upper boundaries of decision variables respectively.

Particle swarm optimization (PSO) is an evolutionary technology based on swarm intelligence, which simulates social behavior. Due to its unique search mechanism, excellent convergence performance and convenient computer implementation, PSO has been widely used in the field of engineering optimization. MOPSO, whose mathematical model can also be simply described by Eq. (13), is a generalization of PSO, the Pareto front of two objectives is obtained at last. The basic steps of MOPSO are as follows:

1) Initialize the particle population and non-dominated solution set;
2) Update the population of particles;
3) Update the non-dominated solution set;
4) Update the optimal solution of each particle according to the update strategy;
5) Judge whether the termination conditions are met.

As a whole, the steps of the multi-objective optimization method for coil current waveform of transcranial magnetic stimulation are shown in Fig. 1.

3. Theoretical optimization results

3.1. Reference waveform

In this paper, the reference full-sine, rectified sine and half-sine current waveforms are selected as the reference current waveforms [39]. The rectified sine, which is not very common, is a waveform for exploration, and is used to compare with the other two of the

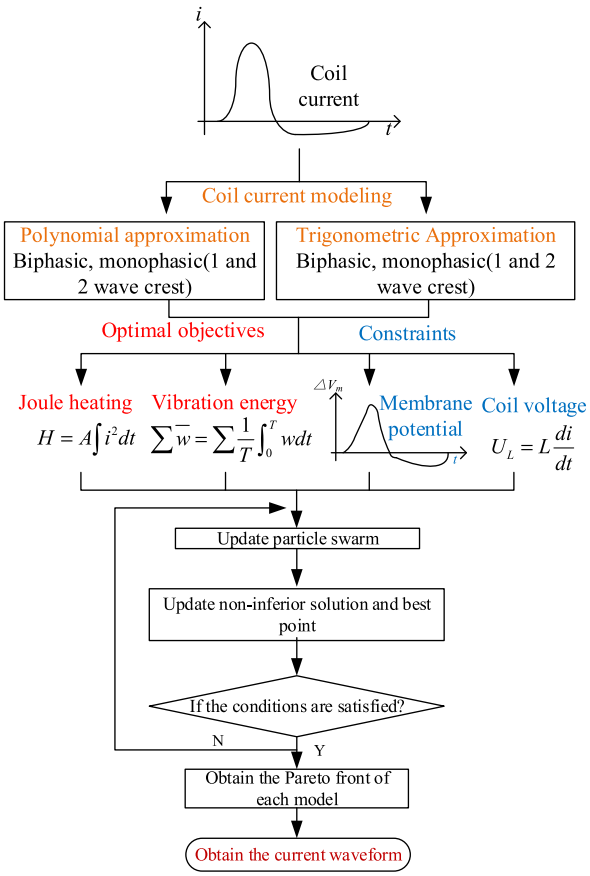

Fig. 1. The overall steps of the proposed optimization method.

same pulse widths to investigate the effect of the difference in waveform shape on each index. The pulse width (PW) of the reference waveforms is set as 400 μs. This value is inspired by the optimization results of [29], the pulse width of which are wider than the common ones. Longer pulse widths can sometimes reduce the maximum coil voltage required to reach a specified stimulus intensity, improving the achievability of optimized waveforms. Therefore, the reference pulse width is chosen to be 400 μs, which is probably larger than the common pulse width. Of course, this is only a benchmark, and can be adjusted according to the specific situation if needed. In addition, perhaps unlike the common case where the half-sine pulse width is half of the full-sine pulse width, the two are set equal in this paper. Because the variable of interest in this optimization method is the shape of the waveform, and in order to ensure a single variable during the study, we make the variable of pulse width consistent across the reference waves. The coil voltage is calculated according to Eq. (8). The intracranial induced electric field is directly proportional to the coil voltage, so the intensity of the induced electric field is directly proportional to di/dt. The amplitude of membrane potential is obtained by the method described above. The normalized current waveforms, intracranial induced electric field and neuronal membrane potential (assuming that the resting potential is 0) are shown in Fig. 2.

According to Eq. (1), the Joule heating of the TMS coil generated by the reference current waveforms is calculated. The vibration energy is also calculated by Eqs. (2)–(7).

Other parameters are shown in Table 1. In the subsequent optimization, the maximum amount of membrane potential of the optimized waveform should be larger than the reference waveform. Due to the different shape of waveforms, the optimized waveforms calculated by Model.1a/2a, Model.1b/2b and Model.1c/2c are compared with the reference full-sine, rectified sine and monophasic half-sine respectively. Fig. 3 shows a set of Pareto fronts for all models considering the dual optimization objectives. The optimization results of each reference waveform under different models are introduced in the following part.

3.2. Piecewise polynomial fitting (Model.1a/1b/1c)

Model.1a/1b/1c are used as the waveform fitting model in this part. The initial parameters of MOPSO: the population size is 200, the repository size is 100, and the number of iterations is 200. Taking the solution results of Model.1a as an example, the Pareto front of the last iteration is shown in Fig. 4. The abscissa of the blue dotted line is 1.9205, i.e., the Joule heating of the reference full-sine waveform (the vibration energy is 1.74, which is greater than the upper limit of the axis in Fig. 4). In fact, all the solutions on the

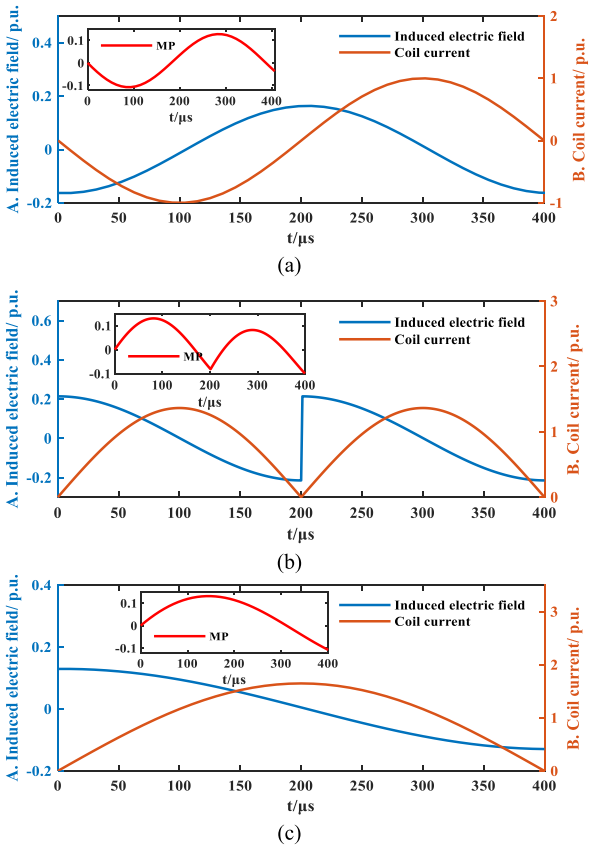

Fig. 2. The waveforms of current, intracranial induced electric field and membrane potential (the reference current) (a) reference full-sine; (b) reference rectified sine; (c) reference half-sine. (Neuronal membrane parameter: $\tau_m = 150$ μs)

Table 1
Parameters of reference Currents (Unit:p.u.).

Type	PW/μs	Max. current	Membrane potential (MP) amplitude	Max. U_L	Joule heating	Vibration energy
Full-sine	400	1.0000	0.1300	0.1571	1.9205	1.7411
Rectified sine	400	1.3645	0.1300	0.2143	3.5748	6.4249
Half-sine	400	1.7717	0.1300	0.1391	6.0267	2.5943

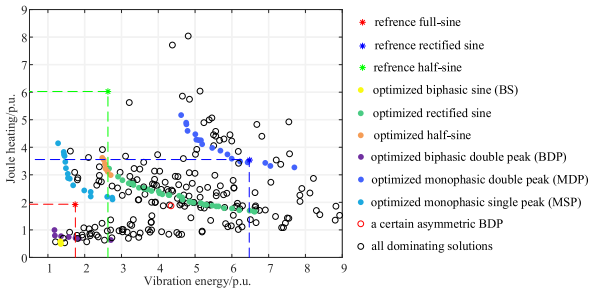

Fig. 3. All Pareto fronts (The red, blue and green dashed lines represent the distribution range of the solutions superior to the reference waveforms.).

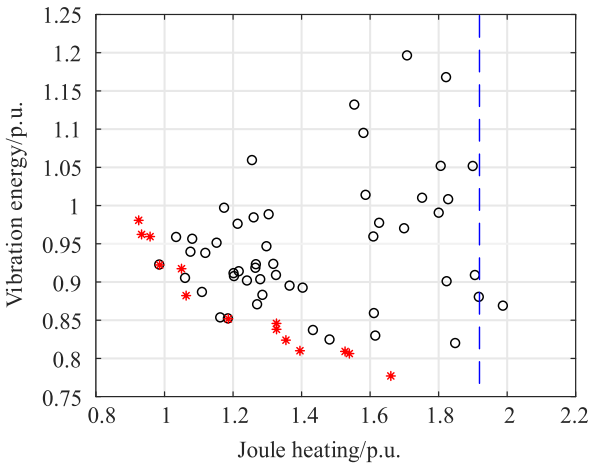

Fig. 4. Pareto front of Model.1a (in the last iteration).

left side of the blue dashed line are better than the reference full-sine current. The black circle is part of the dominated solutions, the red asterisk is the non-dominated solutions. The set of all non-dominated solutions is the Pareto front during this iteration.

The Pareto fronts of Model.1b and Model.1c are also obtained. Taking one of the non-dominated solutions as an example, the optimized coil current, intracranial induced electric field and membrane potential waveforms of Model.1a/1b/1c are shown in Fig. 5, other relevant parameters are shown in Table 2.

The negative amplitude of the optimized BDP (Model. 1a) current (Fig. 5(a)) reaches 0.7034 at $t = 229$ μs, the positive amplitude reaches 0.7118 at $t = 312$ μs. The current pulse width of optimized BDP is 479 μs. Different from the reference waveform, the current waveform of optimized BDP is not completely symmetrical. The amplitude of the optimized BDP current is 28% lower than that of the reference full-sine. In other words, if the maximum current of the reference full-sine is 3000 A, the maximum current of the optimized BDP is only 2160 A. Besides, the Joule heating reduces by 50%, while the vibration energy reduces by 45%. From the perspective of the current waveform, the optimized BDP current can greatly reduce the Joule heating and vibration energy of the coil, thus reducing the heat and clicking noise of the coil.

The optimized MDP (Model. 1 b) current waveform (Fig. 5(b)) is asymmetric. The maximum current of the first peak is 0.4731 at $t = 427$ μs, the pulse width of the first peak is 468 μs. The maximum current of the second peak is 1.7 at $t = 573$ μs, the pulse width of the first peak is 384 μs. Compared with the reference rectified sine, the Joule heating is reduced by 11%, and the vibration energy is reduced by 5%. The overall pulse width of the optimized MDP waveform reaches 811 μs, hence the coil voltage decreases by 19%.

The maximum current of the optimized monophasic single peak (MSP) waveform (Fig. 5(c)) is 1.441 at $t = 156$ μs, and the current pulse width is 322 μs. Due to the decrease in pulse width, the coil voltage increases slightly. However, the maximum current of

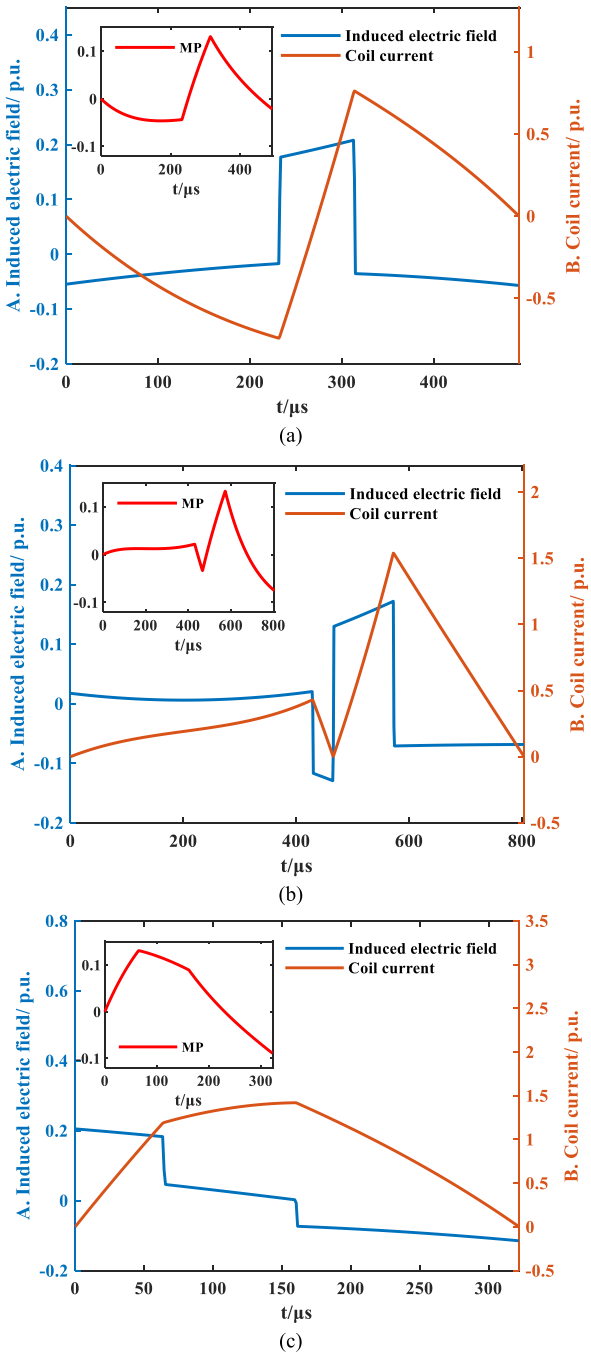

Fig. 5. The waveforms of current, intracranial induced electric field and membrane potential (a) optimized BDP; (b) optimized MDP; (c) optimized monophasic single peak (MSP).

Table 2
Parameters of optimized waveform by Model.1a/1b/1c (Unit:p.u.).

Type	PW/μs	Max. current	Membrane potential (MP) amplitude	Max. U_L	Joule heating	Vibration energy
Optimized BDP	479	0.7118	0.1305	0.1961	0.9594	0.9579
Optimized MDP	811	1.700	0.1328	0.1841	3.3623	6.371
Optimized MSP	322	1.441	0.1305	0.2066	3.2292	1.4974

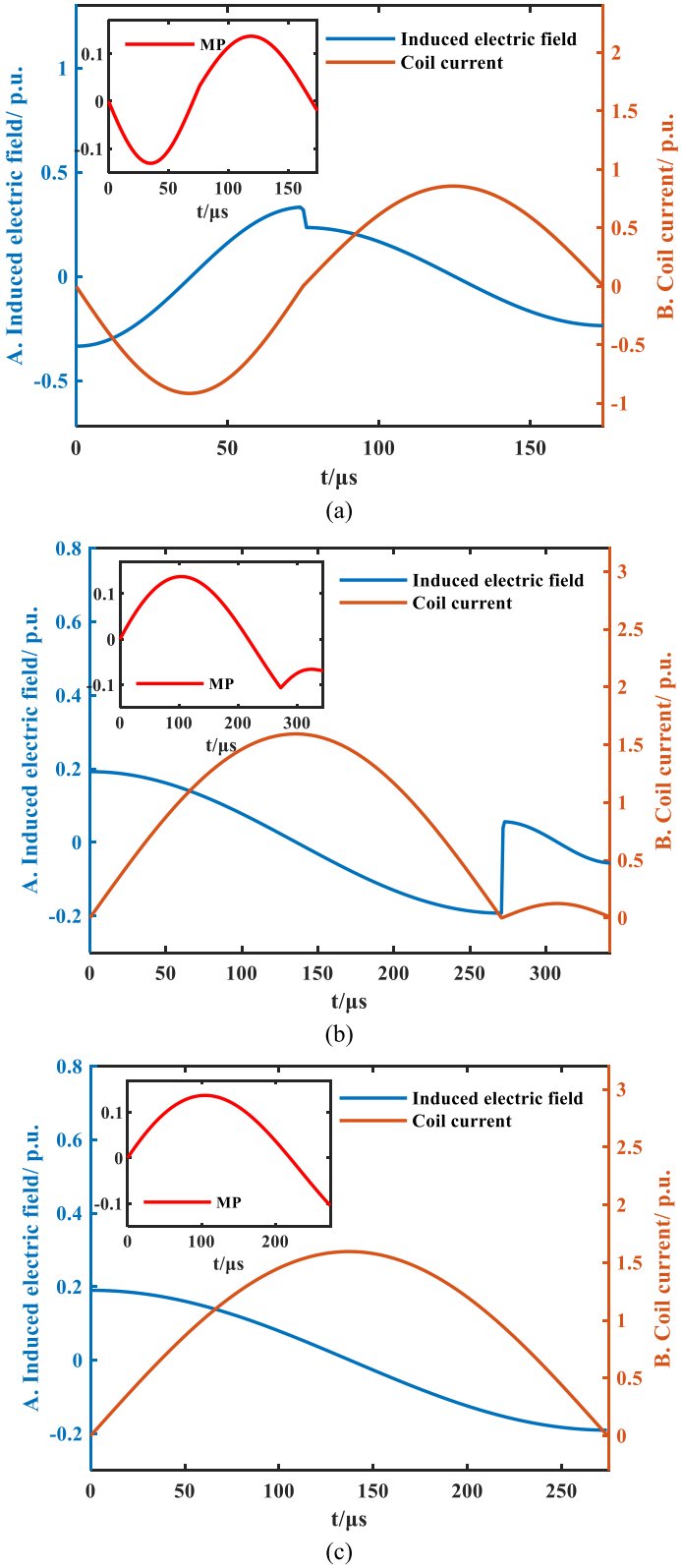

Fig. 6. The waveforms of current, intracranial induced electric field and membrane potential (a)optimized biphasic sine; (b) optimized rectified sine; (c) optimized half-sine.

optimized monophasic single peak (MSP) is 30% less than the reference half-sine. The Joule heating and vibration energy also decreased by 61% and 47%, respectively.

3.3. Trigonometric fitting (Model.2a/2b/2c)

The initial condition of MOPSO is the same as that of the piecewise polynomial fitting for the trigonometric fitting. The Pareto fronts of optimized biphasic sine, rectified sine and half-sine are obtained by using Model.2a/2b/2c, respectively. The waveforms of coil current intracranial induced electric field and membrane potential corresponding to a certain non-dominated solution of Model.2a/2b/2c are shown in Fig. 6, other relevant parameters are shown in Table 3.

Different from the reference full-sine waveform, the optimized biphasic sine waveform (Fig. 6(a)) has two different peaks. The pulse width of the negative peak is 73 μs, the maximum current is 0.8233; the pulse width of the positive peak is wider, which is 97 μs, and the maximum current is 0.7901. In this case, the Joule heating and vibration energy are reduced by 71% and 23% respectively compared with the standard full-sine. However, since the overall pulse width is only 170 μs, the maximum coil voltage is increased. Since the waveform optimization in this paper is not limited to a specific circuit structure, and there are designs with modular structures to achieve higher coil voltages [38], the upper limit of the voltage constraint is set relatively high in the optimization process for the purpose of reducing the limitations on the waveform optimization results. The upper limit of the voltage constraint can be adjusted or lowered according to the actual situation if a more explicit circuit parameter limit is existed based on the reality when using the method in this paper.

From Fig. 6(b), it is obvious that the first peak of the optimized rectified sine current is much larger than the second peak. The maximum current of the first peak is 1.647, while the pulse width is 267 μs. The maximum current of the second peak is only 0.1265, and the pulse width is 86 μs. In fact, the waveform trend of other Pareto front solutions is almost the same. Compared with the reference rectified sine waveform, the Joule heating and vibration energy are reduced by 6% and 61%, respectively. The maximum voltage of the coil is decreased by 13%.

The pulse width of optimized half-sine (Fig. 6(c)) is 275 μs, The Joule heating and vibration energy is 57% and 9% less than that of the reference half-sine waveform. The maximum voltage of the coil is increased by 21%.

4. Optimization results discussion

According to the analysis, the biphasic current has more advantages than monophasic current by taking the Joule heating and vibration energy into consideration. For biphasic current, most of the energy is returned to the circuit because the second peak is opposite to the first peak, avoiding excessive consumption of the remaining energy on the coil. As for monophasic current, because the current decays slower, it generates more heat and vibration energy on the coil than the biphasic current. Nevertheless, the monophasic current has stronger short-term effects than the biphasic current in some cases of rTMS. The monophasic current pulses preferentially activate one group of neurons in the same direction, so the stimulation effects are easy to superimpose. On the contrary, the biphasic current pulse may activate several different groups of neurons, the effect is not as clear as the monophasic current [40]. Consequently, it is difficult to explain which type of current waveform (biphasic or monophasic) is better as a whole.

In addition, the waveforms of the intracranial induced electric field generated by different currents are different. At present, there is no direct relationship between the stimulation effect and the intracranial induced electric field, but different types of the intracranial induced electric field are able to enrich the diversity of TMS stimulation. In Fig. 2(a) and (b), the waveforms of the intracranial induced electric field are almost smooth continuous curve; in Fig. 2(c), the intracranial induced electric field reaches the minimum value at the zero-crossing point of the current. In Fig. 5(b), the intracranial induced electric field is a biphasic near-rectangular waveform; in Fig. 5(c), the intracranial induced electric field is a stepped waveform with different values. In Fig. 6(b), two attenuated peaks with different magnitude and amplitude of intracranial induced electric field are generated. To sum up, on the one hand, the Joule heating and vibration energy of the coil are reduced by optimizing the current waveforms, on the other hand, the diversity of the intracranial induced electric field is greatly enriched.

A more detailed comparison of the optimization results might have led to more instructive suggestions. In Fig. 6(a), the current waveform is similar to the reference full-sine waveform in Fig. 2(a), but the intracranial induced electric field waveform of Fig. 6(a) has a “spike” due to different pulse width and amplitude of peaks. This inconsistency is more evident when the polynomial is used as the basis for fitting as shown in Fig. 5(a), the intracranial induced electric field is a monophasic near-rectangular waveform. From Fig. 3, the optimized biphasic sine (BS) (yellow dot) and the optimized BDP (purple dot) can achieve the best effect. Their common feature is that the two peaks are approximately but not completely symmetrical. This may be due to the fact that the rising edge of the current contributes more to the peak generation of MP [39]. This guides us to improve the flexibility of our existing TMS product waveforms, which means upgrading the stimulus circuit, for example, by using a dual-capacitor structure with different capacitance voltages to

Table 3
Parameters of optimized waveform by Model.2a/2b/2c (Unit:p.u.).

Type	PW/μs	Max. current	Membrane potential (MP) amplitude	Max. U_L	Joule heating	Vibration energy
Optimized biphasic sine	170	0.8322	0.1370	0.3508	0.5532	1.337
Optimized rectified sine	353	1.6468	0.1375	0.1985	3.5324	2.6192
Optimized half-sine	275	1.6537	0.1371	0.1969	3.6023	2.5668

generate an asymmetric induced electric field, as Ref. [9] does, which helps us to better achieve the set multi-objective optimization goals. It should be noted that, this degree of asymmetry is not the larger the better, because we are limited by the two optimization objectives together. For example, the red circle in Fig. 3 represents a biphasic double waveform that the second peak (amplitude: 1.46, pulse width: 270 μs) is significantly larger than the first peak (amplitude: −0.30, pulse width: 62 μs). It can be found that the Joule heating is less than the reference full-sine, but the vibration energy is much larger. However, one peak of the optimized waveform might be obviously larger than the opposite peak if the Joule heating is taken as the optimization objective only [19].

We can also find that generally the narrower the pulse width corresponds to less heat generation. When the MP reaches the set value, if the current drop quickly, the heat can be effectively reduced. However, too narrow a pulse width may result in the need for a larger magnitude of current to produce a stimulus of sufficient intensity, increasing the vibration energy instead. The optimization process in this paper does not focus on the influence of pulse width on the stimulation effect [9,41], mainly because the influence of pulse width is also related to the choice of rTMS protocol [42], and this paper temporarily only focuses on the stimulation intensity index of a pulse waveform, as done in Ref. [9,36,37]. However, this influence will be taken into account in further studies.

To sum up, the multi-objective optimization method for coil current waveform of transcranial magnetic stimulation proposed in this paper is able to obtain several different optimized waveforms which aims at reducing the joule heating and vibration energy. It can reduce the energy dissipation at its root and has certain research value in optimizing the current and providing diverse electric field waveforms of TMS. It can also provide guiding suggestions for stimulus circuit construction.

5. Experiment validation

A proof-of-principle experimental platform is built to prove the realizability of the proposed optimization method for coil current waveform. Fig. 7 shows a diagram of the main circuit elements of the device, and the experiment platform is shown in Fig. 8. A 32 μH figure-of-eight coil is connected to the energy-storage capacitors C_1 (600 μF) and C_2 (2000 μF) through two half-bridge circuits, each of which is implemented with the FF300R17KE3 IGBT-module [9]. High current in practical applications can be achieved by selecting IGBT-modules with higher ratings. The TMS320F28335 control card is used as the controller. A ringing suppression snubber circuit is designed for each half-bridge to reduce the common ringing at the end of the waveform in such pulse width controllable TMS (cTMS). Hence, waveform fitting can be achieved more accurately, and unnecessary heating can be reduced by this ringing suppression-cTMS (RS-cTMS). By adjusting the switching sequence and the charging voltage of the two capacitors, the required coil voltage waveform can be achieved. Consequently, the induced electric field which is proportional to the coil voltage, fitted by the aforementioned model can be realized.

Since the waveform fitted by trigonometric function can be realized by existing products, the waveform in Fig. 5(a) with the best optimization effect (optimized BDP) is selected for experimental verification, and other waveform fitted by piecewise polynomial can be obtained similarly. Fig. 9 illustrates the normalized waveform of the optimized BDP current implemented with the experimental platform and the corresponding coil voltage which is proportional to the induced electric field.

The initial energy-storage capacitor voltages are VC1 = 150 V and VC2 = 38 V. The pulse consists of coil voltage steps of −VC2, VC1, and −VC2, the end time of each step is respectively 229 μs, 312 μs and 481 μs [9].

The change of membrane potential, joule heating and vibration energy caused by the experimental waveform are calculated after normalization, and the results are presented in Table 4 and Fig. 10. Under the same stimulation effect, most indexes of the experimental optimized BDP waveform are much lower than the full-sine counterparts, validating the advantages of the proposed BDP waveform.

The pulse width and the current amplitude of theoretical and experimental waveforms are quite close, with an error within 2%. The error can be further eliminated by adjusting the storage capacitance value and the inductance value of the stimulus coil. Although both the current amplitude and pulse width are larger than the theoretical calculation, the actual heating is slightly smaller. It is mainly because that the current change rate of the third step in the actual discharge process is decreasing, hence, the integral value of the current square of this step is smaller than the theoretical calculation. Vibration energy is bigger because it is proportional to the biquadrate of current amplitude. Additionally, the high-frequency oscillation caused by the parasitic parameters in the experiment circuit also increases the vibration energy. Similarly, the high-frequency vibration increases the peak voltage of the coil, but the maximum voltage recorded in Table 4 refers to the coil voltage that has a practical effect on stimulating the cell after being filtered by the equivalent filter of the membrane.

Above experiment results prove that the stimulation waveform fitted by the optimization method can be physically realized. Moreover, compared with the already-existing stimulation waveform, the fitted waveform can indeed optimize the joule heating and vibration energy under the same stimulation effect.

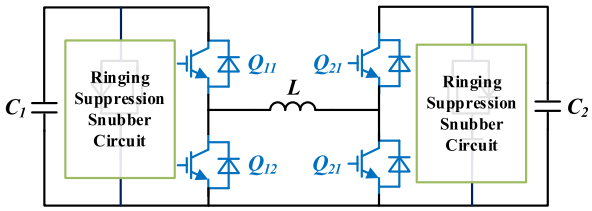

Fig. 7. Diagram of main elements of the experimental platform.

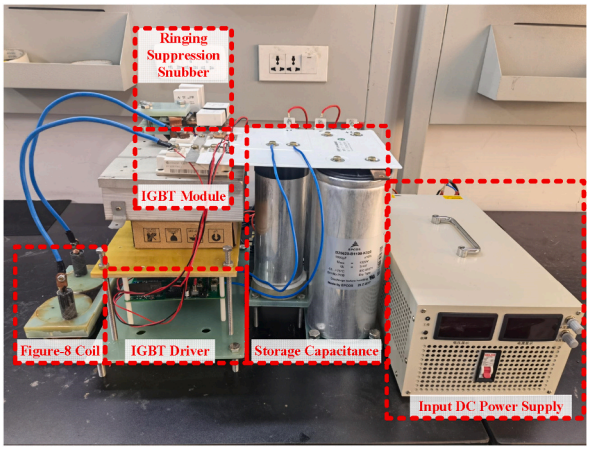

Fig. 8. The experimental platform of ringing suppression-cTMS (RS-cTMS).

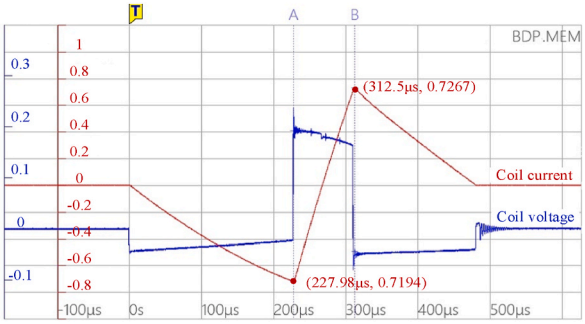

Fig. 9. The normalized experimental waveform of optimized BDP current and coil voltage.

Table 4
Parameters of experimental Optimized Waveform by Model.1a (Unit:p.u.).

Type	PW/μs	Max. current	Membrane potential (MP) amplitude	Max. U_L	Joule heating	Vibration energy
Full-sine	400	1	0.1300	0.1571	1.9205	1.7411
Optimized BDP	479	0.7118	0.1305	0.1961	0.9594	0.9579
Experimental optimized BDP	481	0.7267	0.1310	0.1913	0.9443	1.1503

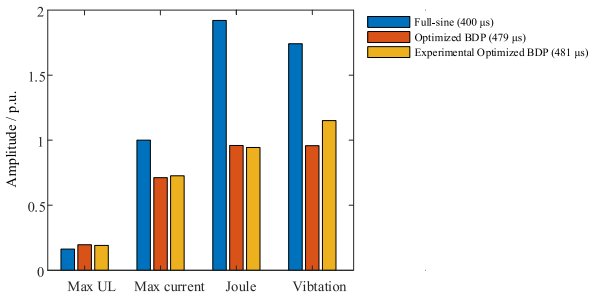

Fig. 10. Comparison of experimental optimized BDP and theory waveform.

6. Conclusion

This paper presents a more implementation-friendly multi-objective waveform optimization method to improve heat and noise problems at the same time, and guide the TMS circuit construction. The waveform parameterization is carried out with considerations

more specific to TMS. Firstly, the relationships between the TMS current and the Joule heating and vibration energy of the coil are constructed, and the commonly used current waveforms are classified and modeled. The Pareto fronts satisfying the optimization objectives are solved by using the MOPSO algorithm. The optimized current waveforms are deduced and analyzed. Finally, the feasibility of the current waveform obtained by the proposed method is validated through experiments. The results show that the Joule heating and vibration energy produced by the optimized BDP current constructed by Model.1a are the least. The optimized waveforms constructed by other current models also perform better than the reference current waveforms. Besides, the optimized current waveforms generate a variety of different intracranial induced electric field waveforms, which provide references for improving the diversity of TMS.

It should be noted that the optimization results in this paper are based on a particular coil structure, and the optimization results obtained may differ depending on the coil structure, as the coil structure can have an impact on the noise level. Hence, the method in this paper can also be used as a part of iterative optimization of coils and waveforms. After determining the basic parameters of the waveform under a specific optimization objective using the optimization method in this paper, the coil structure can be designed for the waveform [43], and then the parameters related to the coil can be brought back to the optimization algorithm to further optimize the waveform. In future research, we plan to take the influence of pulse width on the stimulation effect into consideration for optimization and work on building prototypes with power levels sufficient to achieve TMS for further validation of the optimization method.

Author contribution statement

Ziqi Zhang: Conceived and designed the experiments; Performed the experiments; Analyzed and interpreted the data; Wrote the paper.

Chang Liu: Conceived and designed the experiments; Performed the experiments; Analyzed and interpreted the data; Wrote the paper.

Jihui Hu: Conceived and designed the experiments.

Hongfa Ding: Conceived and designed the experiments.

Zhou He: Performed the experiments.

Yongxiu Song: Contributed reagents, materials, analysis tools or data.

Jiannan Shao: Contributed reagents, materials, analysis tools or data.

Dandi Zhang: Contributed reagents, materials, analysis tools or data.

Funding statement

This work was supported by the National Natural Science Foundation of China [51821005].

Data availability statement

Data will be made available on request.

Declaration of interest's statement

The authors declare no competing interests.

References

[1] J.A. Camacho-Conde, et al., Brain stimulation: a therapeutic approach for the treatment of neurological disorders, CNS Neurosci. Therapeut. 28 (1) (2021) 5–18.
[2] M.D. Johnson, et al., Neuromodulation for Brain Disorders: Challenges and Opportunities, IEEE Trans. Biomed. Eng. 60 (3) (2013) 610–624.
[3] C. Spampinato, et al., Transcranial magnetic stimulation in the assessment of motor cortex excitability and treatment of drug-resistant major depression, IEEE Trans. Neural Syst. Rehabil. Eng. 21 (3) (2013) 391–403.
[4] S.R.D. Best, D.G. Pavel, N. Haustrup, Combination therapy with transcranial magnetic stimulation and ketamine for treatment-resistant depression: a long-term retrospective review of clinical use, Heliyon 5 (8) (2019), e02187.
[5] M. Esposito, et al., In vivo evidence of cortical amyloid deposition in the adult form of Niemann Pick type C, Heliyon 5 (11) (2019), e02776.
[6] V. Walsh, et al., Transcranial magnetic stimulation and cognitive neuroscience, Nat. Rev. Neurosci. 1 (1) (2000) 73–79.
[7] X. Fang, H. Ding, Y. Huang, J. Zhou, Q. Wang, Z. Zhao, Improved intracranial induced electrical field in transcranial magnetic stimulation with semiellipse coil pair, IEEE Trans. Appl. Supercond. 28 (3) (2018) 1–6. Art no. 4901306.
[8] R. Jiang, B.H. Jansen, B.R. Sheth, J. Chen, Dynamic multi-channel TMS with reconfigurable coil, IEEE Trans. Neural Syst. Rehabil. Eng. 21 (3) (2013) 370–375.
[9] A.V. Peterchev, et al., Controllable pulse parameter transcranial magnetic stimulator with enhanced circuit topology and pulse shaping, J. Neural. Eng. 11 (5) (2014), 056023.
[10] N. Gattinger, G. Moßnang, B. Gleich, flexTMS—a novel repetitive transcranial magnetic stimulation device with freely programmable stimulus currents, IEEE Trans. Biomed. Eng. 59 (7) (2012) 1962–1970.
[11] Z. Kagan, et al., Reduced heat generation during magnetic stimulation of rat sciatic nerve using current waveform truncation, IEEE Trans. Neural Syst. Rehabil. Eng. 27 (5) (2019) 937–946.
[12] P.Y. Ktonas, T. Penzel, G. Ruffini, Guest editorial: special issue on noninvasive electromagnetic brain stimulation, IEEE Trans. Neural Syst. Rehabil. Eng. 21 (3) (2013) 331–332.
[13] S.C. Dhamne, et al., A measure of acoustic noise generated from transcranial magnetic stimulation coils, Brain Stimul. 7 (3) (2014) 432–434.
[14] S. Tringali, et al., Related noise exposure and auditory consequence during transcranial magnetic stimulation: new insights and review of the literature, Neurophysiol. Clin. – Clin. Neurophysiol. 43 (1) (Jan 2013) 19–33.

[15] C.C.M. Angel, et al., Transcranial magnetic stimulation and acoustic trauma or hearing loss in children, Neurol. Res. 23 (4) (2001) 343–346.
[16] S.M. Goetz, et al., Impulse noise of transcranial magnetic stimulation: measurement, safety, and auditory neuromodulation, Brain Stimul. 8 (1) (2015) 161–163.
[17] H.R. Siebner, et al., Imaging functional activation of the auditory cortex during focal repetitive transcranial magnetic stimulation of the primary motor cortex in normal subjects, Neurosci. Lett. 270 (1) (1999) 37–40.
[18] Sameer C. Dhamne, et al., A measure of acoustic noise generated from transcranial magnetic stimulation coils, Brain Stimul. 7 (3) (2014) 432–434.
[19] P. Braun, et al., Coil efficiency for inductive peripheral nerve stimulation, IEEE Trans. Neural Syst. Rehabil. Eng. 30 (2022) 2137–2145.
[20] C.M. Epstein, et al., Iron-core coils for transcranial magnetic stimulation, J. Clin. Neurophysiol. 19 (4) (2002) 376–381.
[21] C. Liu, et al., Optimal design of transcranial magnetic stimulation thin core coil with trade-off between stimulation effect and heat energy, IEEE Trans. Appl. Supercond. 30 (4) (2020).
[22] M. Belyk, et al., Accessory to dissipate heat from transcranial magnetic stimulation coils, J. Neurosci. Methods 314 (2019) 28–30.
[23] X. Fang, et al., Optimum design of continuously workable transcranial magnetic stimulator, IEEE Trans. Appl. Superconduct. 30 (4) (2020).
[24] A.V. Peterchev, et al., Quiet transcranial magnetic stimulation: status and future directions, IEEE Eng. Med. Biol. Soc. Conf. Proc. (2015) 226–229.
[25] L.M. Koponen, et al., Double-containment coil with enhanced winding mounting for transcranial magnetic stimulation with reduced acoustic noise, IEEE Trans. Biomed. Eng. 68 (7) (2021) 2233–2240.
[26] C.C. Sanchez, et al., Solving an IBEM with supporting vector analysis to design quiet TMS coils, Eng. Anal. Boundary Elem. 114 (2020) 1–12.
[27] A.V. Peterchev, D.L.K. Murphy, S.M. Goetz, Quiet transcranial magnetic stimulation: status and future directions, in: 2015 37th Annual International Conference of the IEEE Engineering in Medicine and Biology Society (EMBC), Milan, 2015, pp. 226–229.
[28] C. Liu, et al., Noise analysis and active noise control strategy of transcranial magnetic stimulation device, AIP Adv. 9 (8) (2019).
[29] S.M. Goetz, et al., Analysis and optimization of pulse dynamics for magnetic stimulation, Plos One 8 (3) (2013), e55771.
[30] R.F. Yu, et al., A review on cognitive waveform optimization for different radar missions, Acta Electron. Sin. 50 (3) (2022) 726–752.
[31] C.A.C. Coello, et al., MOPSO: a proposal for multiple objective particle swarm optimization, IEEE Congr. Evolut. Comput. (2002) 1051–1056.
[32] X. Xu, et al., Optimized sizing of a standalone PV-wind-hydropower station with pumped-storage installation hybrid energy system, Renew. Energy 147 (2020) 1418–1431.
[33] K.M. Dempsey, H.M. Irvine, A note on the numerical evaluation of Duhamel's integral, Earthq. Eng. Struct. Dynam. 6 (5) (1978) 511–515.
[34] L. Guevremont, C.G. Renzi, J.A. Norton, J. Kowalczewski, R. Saigal, V.K. Mushahwar, Locomotor-related networks in the lumbosacral enlargement of the adult spinal cat: activation through intraspinal microstimulation, IEEE Trans. Neural Syst. Rehabil. Eng. 14 (3) (2006) 266–272.
[35] N. Bhadra, K.L. Kilgore, Direct current electrical conduction block of peripheral nerve, IEEE Trans. Neural Syst. Rehabil. Eng. 12 (3) (2004) 313–324.
[36] A.V. Peterchev, et al., Repetitive transcranial magnetic stimulator with controllable pulse parameters, J. Neural. Eng. 8 (3) (2011), 036016.
[37] A.V. Peterchev, et al., A transcranial magnetic stimulator inducing near-rectangular pulses with controllable pulse width (cTMS), IEEE Trans. Biomed. Eng. 55 (1) (2008) 257–266.
[38] Z. Zeng, et al., Modular multilevel TMS device with wide output range and ultrabrief pulse capability for sound reduction, J. Neural. Eng. 19 (2) (2022), 026008.
[39] I. Delvendahl, et al., The role of pulse shape in motor cortex transcranial magnetic stimulation using full-sine stimuli, PLoS One 9 (12) (2014).
[40] Noritoshi Arai, et al., Comparison between short train, monophasic and biphasic repetitive transcranial magnetic stimulation (rTMS) of the human motor cortex, Clin. Neurophysiol. 116 (3) (2005) 605–613.
[41] I. Halawa, et al., Neuronal tuning: selective targeting of neuronal populations via manipulation of pulse width and directionality, Brain Stimul. 12 (5) (2019) 1244–1252.
[42] R. Hannah, et al., Pulse width biases the balance of excitation and inhibition recruited by transcranial magnetic stimulation, Brain Stimul. 12 (3) (2020) 536–538.
[43] L.M. Koponen, et al., Double-containment coil with enhanced winding mounting for transcranial magnetic stimulation with reduced acoustic noise, IEEE Trans. Biomed. Eng. 68 (7) (2021) 2233–2240.